Journal of Biomechanics 82 (2019) 313–323

Contents lists available at ScienceDirect

Journal of Biomechanics

journal homepage: www.elsevier.com/locate/jbiomech
www.JBiomech.com

The influence of model order reduction on the computed fractional flow reserve using parameterized coronary geometries

K. Gashi *, E.M.H. Bosboom, F.N. van de Vosse

Department of Biomedical Engineering, Eindhoven University of Technology, Eindhoven, the Netherlands

ARTICLE INFO

Article history:
Accepted 3 November 2018

Keywords:
Fractional flow reserve
Computational fluid dynamics
Uncertainty quantification
Model order reduction

ABSTRACT

Computational fluid dynamics (CFD) models combined with patient-specific imaging data are used to non-invasively predict functional significance of coronary lesions. This approach to predict the fractional flow reserve (FFR) is shown to have a high diagnostic accuracy when comparing against invasively measured FFR. However, one of the main drawbacks is the high computational effort needed for preprocessing and computations. Hence, uncertainty quantification may become unfeasible. Reduction of complexity is desirable, computationally inexpensive models with high diagnostic accuracy are preferred. We present a parametric comparison study for three types of CFD models (2D axisymmetric, Semi-3D and 3D) in which we study the impact of model reduction on three models on the predicted FFR. In total 200 coronary geometries were generated for seven geometrical characteristics *e.g.* stenosis severity, stenosis length and vessel curvature. The effect of time-averaged flow was investigated using unsteady, mean steady and a root mean square (RMS) steady flow. The 3D unsteady model was regarded as reference model. Results show that when using an unsteady or RMS flow, predicted FFR hardly varies between models contrary to using average flows. The 2D model with RMS flow has a high diagnostic accuracy (0.99), reduces computational time by a factor 162,000 and the introduced model error is well below the clinical relevant differences. Stenosis severity, length, curvature and tapering cause most discrepancies when using a lower order model. An uncertainty analysis showed that this can be explained by the low variability that is caused by variations in stenosis asymmetry.

1. Introduction

Coronary heart disease is characterized by plaque buildup within the arterial wall resulting in stenoses. Stenoses may impair myocardial perfusion such that myocardial ischemia may occur during exercise or even rest (Stary et al., 1995). To determine the correct treatment for a stenosis, its hemodynamic severity needs to be assessed. This can be done by determining the fractional flow reserve (FFR) which is approximated by the ratio between the (intra-vascular measured) time-averaged pressure distal and proximal to the stenosis (Pijls et al., 1995). In multiple large randomized-control clinical trials FFR is shown to be reliable for classifying stenoses (De Bruyne et al., 2014; Pijls et al., 2007; Tonino et al., 2010). However, measuring FFR is an invasive procedure that needs catheterization. Retrospectively, up to 50% of the catheterizations was unnecessary as these patients only needed medicine treatment (Koo et al., 2011; Min et al., 2012; Nørgaard et al., 2014). Using computational fluid dynamics (CFD) models, the invasive nature of FFR assessment could be omitted (Morris et al., 2013, 2015; Nakazato et al., 2013; Tu et al., 2014). With, in general, 3D CFD models, FFR can be computed based on CT or other imaging data only, hence without the use of intra-vascular pressure measurements. One of the main drawback of these models is the fact that they are computationally expensive (Morris et al., 2017). Depending on the amount of computational resources and simulated physical time, simulations can last somewhere between minutes (Tu et al., 2014) for a steady approach until hours to days for a transient approach (Morris et al., 2017). The 3D approach works straightforward for full 3D scans (CT or MRI) compared to single-plane or bi-plane angiograms where 3D models of vessels need to be reconstructed first (Çimen et al., 2016; Chen and Carroll, 2000). Reconstructing semi-3D geometries using angiographic data for FFR predictions yields promising results as illustrated by Morris et al. (2013). Although the semi-3D approach makes FFR predictions based on angiographic data possible, it still remains computationally expensive (Morris et al., 2017).

* Corresponding author at: Department of Biomedical Engineering, Eindhoven University of Technology, Building 15, PO Box 513, 5600 MB Eindhoven, the Netherlands.

E-mail addresses: K.Gashi@tue.nl (K. Gashi), F.N.v.d.Vosse@tue.nl (F.N. van de Vosse).

https://doi.org/10.1016/j.jbiomech.2018.11.008
0021-9290/

The Semi-3D approach depends on the number of available images and the angle between images. Therefore, stenosis asymmetry might be caused by possible misrepresentation of stenoses resulting from insufficient number of images from single-plane and biplane angiograms. It is not yet clear what the benefit of a full 3D approach is and to what extend a semi-3D approach is accurate enough or if it even can be further reduced to 2D. In previous research the effect of curvature, torsion and stenosis severity has been shown to have an effect on the velocity profiles and wall shear stress (Katritsis et al., 2010; Chang and Tarbell, 1988; Hayashi and Yamaguchi, 2002). To which extend this might affect FFR predictions when applying a reduced order model needs to be investigated.

For an accurate prediction of the FFR, CFD models need to include uncertainty for boundary conditions and geometry. Variation of a few voxels in the lumen segmentation of a stenosis can yield an opposite diagnosis (Sankaran et al., 2015). In a later study, it was shown that myocardial resistance can have a similar impact on the FFR as the minimal lumen diameter (Sankaran et al., 2016). To include uncertainty in CFD models, computational time needs to be minimal to allow for multiple model evaluations. Itu et al. has shown promising results using a reduced order model (Itu et al., 2016). Therefore, we propose a parametric comparison study for three types of CFD models with different complexities which if needed can be extended for example for more accurate representation of non-Newtonian blood viscosity. The first model is the full 3D model which generally results from CT data segmentation (Min et al., 2012; Nørgaard et al., 2014; Taylor et al., 2013). This model resembles the physiological situation the most as it captures most of the geometrical features. The second model is the semi-3D model which is characterized by its symmetric contours along the centerline of the geometry (Morris et al., 2015, 2017; Tu et al., 2014). The semi-3D model results from angiogram data segmentation of the centerline and effective radius. Third is the 2D axisymmetric model which is a simplified semi-3D model. The centerline loses its curvature and torsion and becomes a straightend tube with only one slice from centerline to wall (Morris et al., 2016).

Model complexity is also influenced by whether a model is evaluated for the steady or unsteady case. Evaluating unsteady models increases computational costs as simulations need to be performed until a steady-state solution is achieved.

The goal of this study is to investigate to what extend less complex models can be used while still maintaining their accuracy with respect to 3D models. For this, a large number of parametrized coronaries are constructed for three model types using various geometrical features such as stenosis severity, stenosis length, curvature, tapering, etc. Using uncertainty analysis, the effect of each geometrical feature on the predicted FFR is investigated and quantified features that have the largest effect on the predicted FFR are determined. The uncertainty analysis is expanded to the steady and unsteady case for the models to compare the steady and unsteady approach.

2. Material and methods

2.1. Geometry definition

To quantify the impact of different model assumptions, 200 idealized coronary artery geometries were made. Seven parameters were set for each geometry: stenosis severity, stenosis asymmetry, stenosis length, curvature, torsion, angular stenosis position and tapering. Construction of the geometry was done in five steps. The first step was to create straight tubes with diameter of 2.8 mm and a length of 95 mm which correspond to either left or right coronary arteries (Tu et al., 2014). Symmetric stenoses were added with predefined severities using the following relation see Figs. 1 and 2:

$$s(z)=\frac{r(z)}{r_{ref}}=\begin{cases}1+\frac{1}{2}s_r\left(\cos\left(\frac{\pi}{l_{si}}(z-z_i)\right)-1\right), & \text{if } z_i\leqslant z\leqslant z_i+l_{si}\\ 1-s_r, & \text{if } z_i+l_{si}<z<z_o-l_{so}\\ 1+\frac{1}{2}s_r\left(\cos\left(\frac{\pi}{l_{so}}(z-z_o)\right)-1\right), & \text{if } z_o-l_{so}\leqslant z\leqslant z_o\end{cases} \tag{1}$$

With, s_r representing the stenosis severity expressed in radius reduction. The variable z represents the longitudinal position. Furthermore, the positions and lengths of the stenosis inlet and outlet are given by z and l_s, respectively. Parameters with respect to inlet and outlet are indicated with the subscripts i and o, respectively. Next, the stenosis was moved in radial direction using the asymmetry index which was defined as:

$$a(z)=\begin{cases}r_{ref}\cdot s_r\cdot a_{ref}\cdot\left[\frac{1}{2}-\frac{1}{2}\cos\left(\pi\frac{z-z_i}{l_{si}}\right)\right], & \text{if } z_i\leqslant z\leqslant z_i+l_{si}\\ r_{ref}\cdot s_r\cdot a_{ref}, & \text{if } z_i+l_{si}<z<z_o-l_{so}\\ r_{ref}\cdot s_r\cdot a_{ref}\cdot\left[\frac{1}{2}+\frac{1}{2}\cos\left(\pi\frac{z-z_o-l_{so}}{l_{so}}\right)\right], & \text{if } z_o-l_{so}\leqslant z\leqslant z_o\end{cases} \tag{2}$$

Herein, r_{ref}, a_{ref} are the predefined radius and the asymmetry index. The asymmetric translation of the stenosis is given by:

$$\begin{bmatrix}x(z)\\ y(z)\end{bmatrix}=s(z)\begin{bmatrix}x_0(z)\\ y_0(z)\end{bmatrix}+a(z)\begin{bmatrix}\cos(\theta)\\ \sin(\theta)\end{bmatrix} \tag{3}$$

Herein $x_0(z)$ and $y_0(z)$ are the original coordinates perpendicular to the longitudinal direction whereas $x(z)$ and $y(z)$ correspond to the new deformed coordinates when applying a stenosis and asymmetry. The angular position of the stenosis is given by θ. For the semi-3D geometries no asymmetry is applied such that $a(z)$ remains 0 for all Semi-3D cases.

The third step was to apply curvature and torsion to mimick 3D behavior of coronaries by modifying the centerline using Frenet-Serret formulas:

$$\begin{bmatrix}\mathbf{T}'\\ \mathbf{N}'\\ \mathbf{B}'\end{bmatrix}=\begin{bmatrix}0 & \kappa & 0\\ -\kappa & 0 & \tau\\ 0 & -\tau & 0\end{bmatrix}\begin{bmatrix}\mathbf{T}\\ \mathbf{N}\\ \mathbf{B}\end{bmatrix} \tag{4}$$

Herein **T** and **N** are the vectors tangent and normal to the direction of the centerline, respectively. The binormal vector (**B**) is defined as the cross product of **T** and **N**. Furthermore, the curvature and torsion of the centerline are represented with κ and τ, respectively.

Over the full length of the vessel tapering was applied, meaning the radius along the vessel was reduced by a predefined radius reduction.

3D tetrahedral meshes with boundary layer and finer meshed stenosis were generated using VMTK (Antiga et al., 2008). A full 3D mesh convergence study was performed for an area-reduction of 50% and 90% with mesh sizes of 1.4 and 1.6 million elements, respectively. Number of elements for 3D models ranging between 290,000 and 350,000 were shown to be sufficient as the pressure drop differed less then 2% with respect to the finest meshes. For the 2D models, 4000–7000 elements were needed as the difference in pressure drop was also below 2% compared to the finest mesh of 40,000 elements. For semi-3D models the asymmetry index was zero with the same meshing approach as described above. For 2D models, meshes were created using centerlines and radius profiles of 3D geometries. Centerlines were mapped on a linear coordinate such that the radius profile was a function of the centerline length. 2D axisymmetric meshes with bi-quadratic quadrilateral elements and a boundary layer were created using the finite element software SEPRAN (TU Delft, the Netherlands) (Segal, 1989).

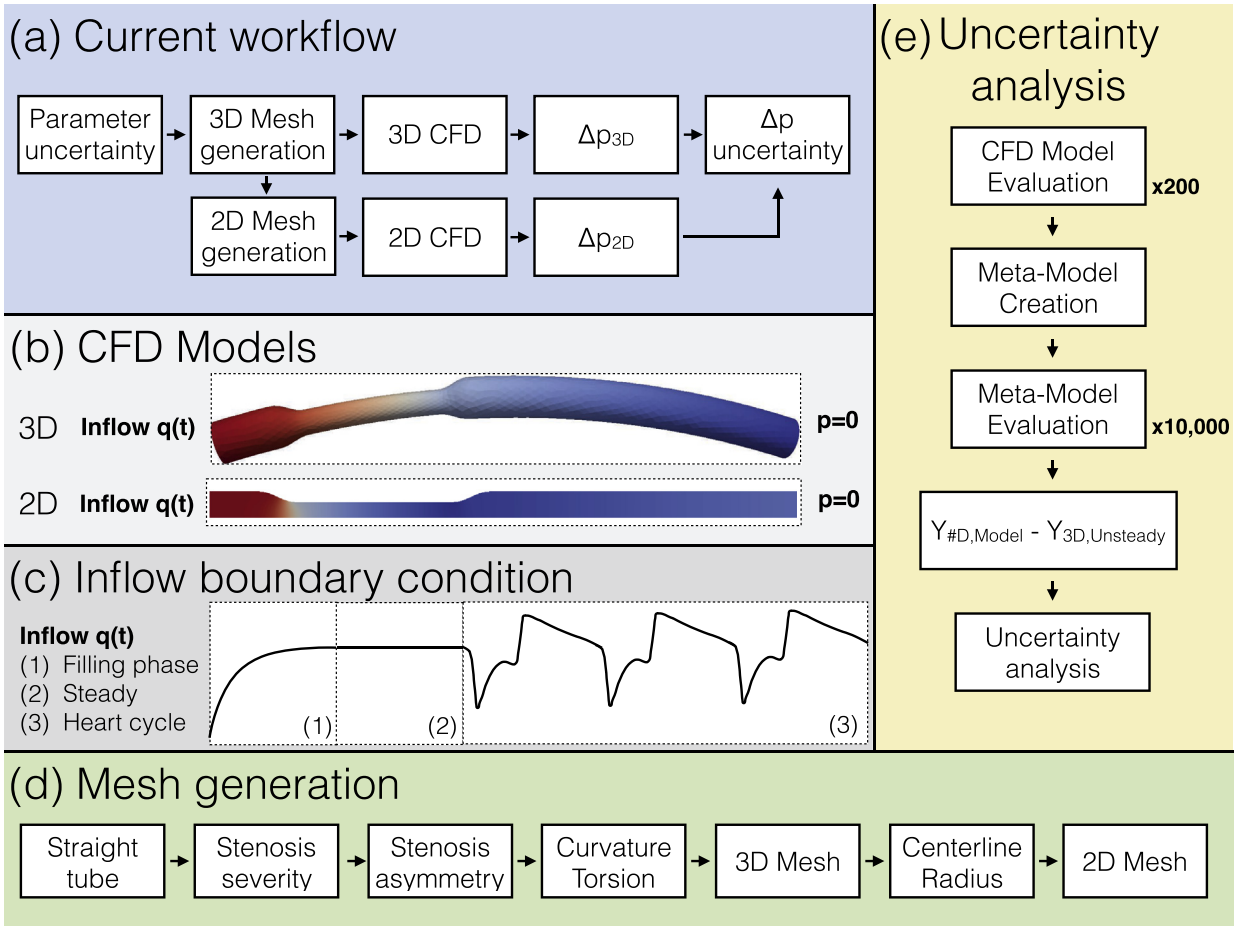

Fig. 1. Schematic overview of the simulation study. In (**a**) based on parameter uncertainty 3D, semi-3D and 2D meshes are generated. The obtained pressures are used to determine which parameter of the geometry influences the pressure drop prediction the most. As shown in (**b**), all CFD models have a stress-free boundary condition at the outlet whereas at the inlet a flow-driven approach is applied. The applied flow (**c**) consists of three parts. A filling phase (1 s) is used to bring the system to the correct flow, the flow is then kept constant for 1.15 s where after four heart cycles (4 s) were imposed. The mesh generation (**d**) starts with a straight tube on which a stenosis severity is imposed. The stenosis can then be located either at the center of the vessel or moved to the outer side of the vessel depending on the asymmetry of the stenosis. Next, the geometry obtains its curvature and torsion based on the Frenet-Serret formulas. Once the 3D mesh is constructed, centerline and radius can be extracted such that a 2D axisymmetric mesh can be constructed. For each model, meta-models (**e**) are generated based on the parameter sets and output of interest. Using these meta-models, a large set of model output is generated based on the properties of the original CFD model. For each model the output is compared against the 3D unsteady model and uncertainty analysis is performed.

2.2. CFD model

For this study, blood flow was governed by the incompressible Newtonian Navier-Stokes equations given as:

$$\rho\left(\frac{\partial \vec{u}}{\partial t} + \vec{u}\cdot\nabla\vec{u}\right) = -\nabla p + \nabla\cdot 2\eta\mathbf{D}, \tag{5}$$

$$\nabla\cdot\vec{u} = 0, \tag{6}$$

with $\vec{u}$ the velocity, p the pressure, and $\mathbf{D}$ the rate of deformation tensor. The dynamic viscosity η is set to be $3.5\cdot10^{-3}$ Pa $\cdot$ s whereas ρ is set at 1050 kg/m^3. For the 3D simulations, Fenics was used in combination with OASIS using the incremental pressure correction method (Alnæs et al., 2015; Mortensen and Valen-Sendstad, 2015). For 2D simulations an in-house finite element package (TFEM) was used (Hulsen, 2007). For the 3D and 2D simulations a time step of 0.1 ms and 1 ms was used, respectively see Fig. 3.

2.3. Boundary conditions

Flow boundary conditions at the inlet were chosen to represent hyperemic flow and to be stenosis dependent. This was done using the non-linear relationship between coronary flow reserve (CFR) and stenosis severity found in literature (Gould, 2009; Miller et al., 1994; Wei et al., 2001). For low severities, CFR and thus flow are invariant to stenosis severity as CFR remains almost constant. For certain stenosis severities CFR decreases exponentially with eventually no blood flow for higher severities. This non-linear behavior was used to derive a severity flow relationship using the following assumptions. (1) Flow was assumed to be only zero for a total occluded blood vessel (Gould, 2009). Although, in the approach of Wei the flow was shown to be zero while still some lumen area remained open, this was assumed to be due to collateral flow (Wei et al., 2001). (2) Flow was also estimated in absence of a stenosis. From the work of for example Min et al. and Kim et al. it can be observed that coronary arteries proximal to the stenosis have a FFR close to 1 (Min et al., 2015; Kim et al., 2014). This means that before blood arrives at the stenosis, it already lost part of its pressure proximal to the stenosis. It was assumed that flow (q_{max}) without stenosis would result in a FFR of 0.95 based on literature (Kim et al., 2014; Min et al., 2015). (3) FFR for a 50% and 90% area reduction stenosis was assumed to be around 0.85–0.9 and 0.6, respectively based on literature (Tonino et al., 2010; Johnson et al., 2013). For this purpose, flows were estimated for two geometries with an area reduction of 50% and 90% (Tonino et al., 2010;

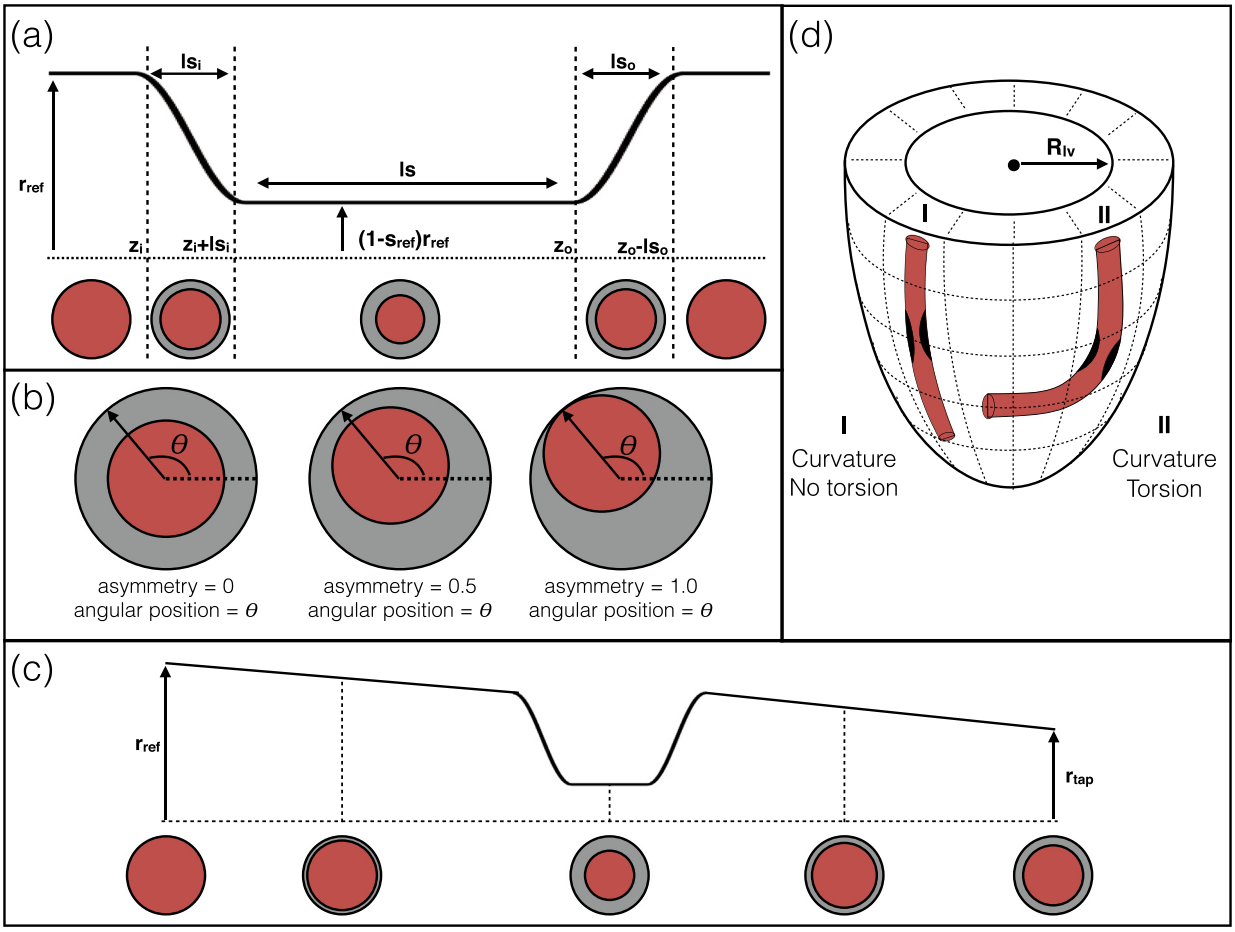

Fig. 2. The definition of all seven parameters used to define the geometries are shown. The lumen is shown in red whereas the original lumen in case of stenosis is shown in grey. An example of a stenosis is shown in (**a**) where the stenosis length and severity are freely varied. The stenosis can then be shifted towards a desired position using a predefined asymmetry and angular position (**b**). Tapering of the vessel (**c**) (continuous radius reduction) is applied to mimick the *in vivo* situation when travelling more distal. Different alignment of coronary arteries is shown in (**d**). Here two distinct cases are shown, only curvature (**I**) and curvature in combination with torsion (**II**).

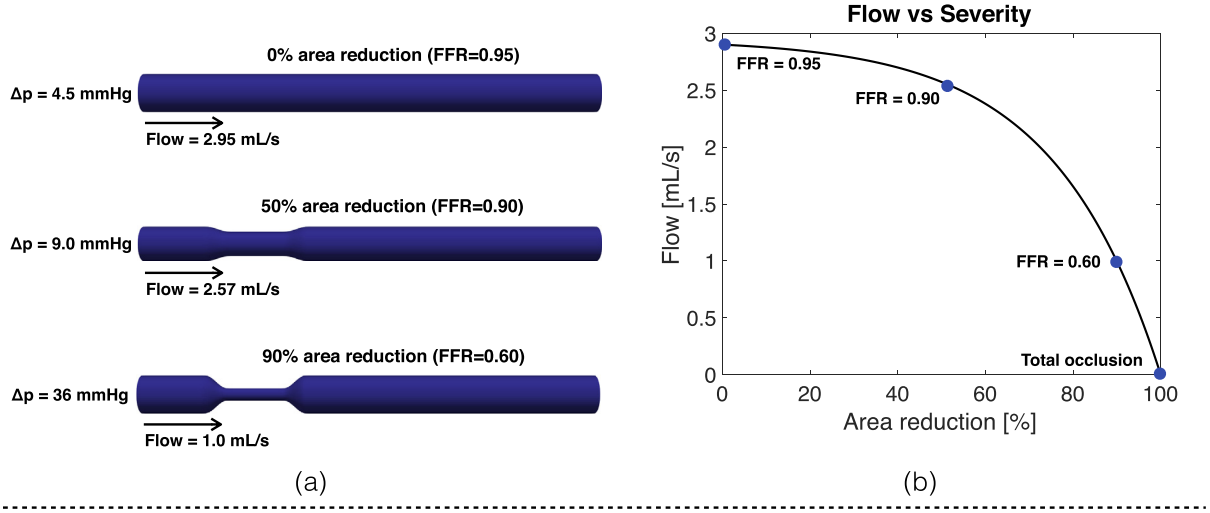

Fig. 3. Obtaining a relationship between flow and stenosis severity by estimating the flow for four different stenosis severities. For this, typical FFR values for different severities were used from literature. In (a) the three geometries for which the flow was estimated are shown. The resulting relation between severity and flow is shown in (b).

Johnson et al., 2013) by increasing the flow until the corresponding FFR was found (Tonino et al., 2010; Johnson et al., 2013). These two flow values (q_{area50}, q_{area90}) in combination with q_{min} and q_{max} were then used to obtain the non-linear relationship between severity (S_A) and the prescribed flow at the inlet (q) of the form: (Gould, 2009; Miller et al., 1994; Wei et al., 2001)

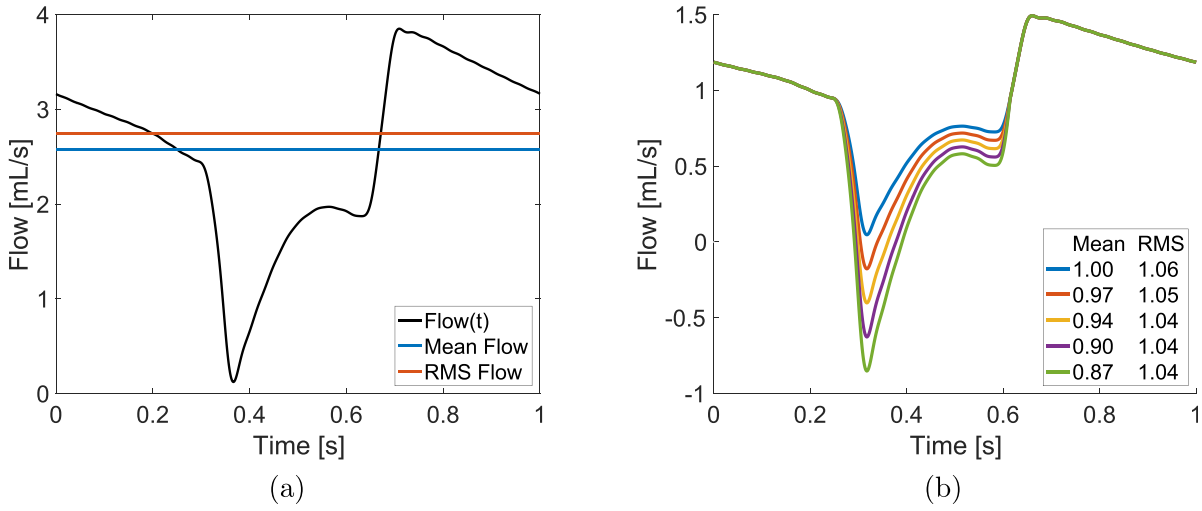

Fig. 4. In (a) an example of a transient flow curve (black) is shown which is applied for the 2D, semi-3D and 3D models. Furthermore, the mean (blue) and root mean square (red) of the flow curve are indicated. An example (b) of changing mean and RMS flow is shown for an increase in regurgitant flow.

$$q = q_{max} \cdot (1 - \exp(-b \cdot S_A)), \tag{7}$$

$$S_A = \frac{A_{stenosis}}{A_{ref}} = \frac{r_{stenosis}}{r_{ref}} = (1 - s_r)^2, \tag{8}$$

where q_{max} and b are the flow without stenosis and an exponential decay constant, respectively. As q_{max} was known, only the decay constant (b) needed to be fitted. This resulted in a non-linear relationship between flow and severity as found in literature with q_{max} and b equal to 2.95 mL/s and 4.119, respectively (Gould, 2009; Miller et al., 1994; Wei et al., 2001). (4) For the transient coronary flow behavior, a typical left coronary flow curve was used with high flow during diastole and low flow during systole (Boron and Boulpaep, 2012; Hall, 2015). The mean of the transient flow curve was scaled using Eq. (7). (5) As for this study flow was prescribed, by definition, the pressure drop was calculated using the Navier-Stokes equation instead of the patient's arterial pressure. Hence for the last assumption the mean arterial pressure was assumed to be 90 mmHg (12 kPa) (Tang et al., 2009; Taylor et al., 2013; Wilson et al., 1988). Using the pressure drop (Δp) and mean arterial pressure ($\overline{p}_a$), the FFR was calculated as follows:

$$FFR = 1 - \frac{\Delta p}{\overline{p}_a}. \tag{9}$$

For the steady simulations both average and root mean square (RMS) of the transient flow signal were used. The mean flow ($\overline{q}$) was used to investigate how well it scales with the predicted FFR which itself is a ratio between the time-averaged pressure distal and proximal to a stenosis (Pijls et al., 1995). The RMS of the flow (q_{rms}) takes into account the shape of the flow signal, weighing the peaks of the signal higher compared to lower values. The equations for mean flow and the RMS flow are given as:

$$\overline{q} = \frac{\sum_{i=1}^{n} q_i}{n}, \tag{10}$$

$$q_{rms} = \sqrt{\frac{\sum_{i=1}^{n} q_i^2}{n}}, \tag{11}$$

here, q_i represents a discrete flow value of the flow signal consisting of n points. In Fig. 4a a coronary flow with corresponding mean and root mean square is shown. The root mean square of the flow for this study was shown to be slightly higher compared to the mean flow. Furthermore, the influence of increased retrograde flow on the mean and root mean square of the flow is shown in Fig. 4b.

For stable simulations, a start-up phase was introduced where the flow was gradually increased for 1 s to either the mean or RMS for the transient flow curve. Next, the inflow was kept constant for 1.15 s to obtain a steady solution. Next, 4 heart cycles of 1 s were imposed.

2.4. Uncertainty analysis

Parameter variation for mesh generation are shown in Table 1. Tonino et al. (2010) showed that stenoses with an area reduction between 50% and 70% were most difficult to distinguish as either functionally significant or non-significant (Tonino et al., 2010). On average 35% of these stenoses were functionally significant. For stenoses with an area reduction between 70% and 90%, approximately 80% of stenoses were functionally significant. In this study the area reduction of stenoses was varied between 50% and 90% as visual assessment of these stenoses did not correspond well to functional assessment (Tonino et al., 2010). In order to capture various kind of asymmetric stenoses, the stenosis asymmetry was varied between perfectly symmetric (0) and fully asymmetric stenosis against the wall (1). The effective stenosis length was varied between 5 and 10 mm similar to what was shown in Tonino et al. (2009) and Sankaran et al. (2016). Both the inlet and outlet of stenosis were kept constant at 2 mm. Waksman et al. (2013) investigated the curvature and cyclic curvature of coronary arteries for 38 patients (Waksman et al., 2013). Therefore, the broadest curvature range was assumed ranging between 0 and 0.887 cm^{-1}. For the torsion of coronary arteries, a left ventricular radius of 3.5 cm

Table 1
Geometrical features used in this study with their corresponding minimum and maximum value.

	Minimum	Maximum
Severity [%]	50	90
Asymmetry [–]	0	1
Length [mm]	5	10
Curvature [cm^{-1}]	0	0.887
Torsion [cm^{-1}]	0	0.286
Angular position [–]	0	2π
Tapering [%]	0	20

was expected. This way the minimum (no circumference alignment) and maximum (pure circumference alignment) torsion ranged between 0 and 0.286 cm^{-1}. Due to the 3D nature of coronary vessels, a stenosis can be located either on the inside of the bend or on the outside. Therefore, the angular stenosis position was varied independently of the curvature and torsion between 0 and 2π radials. For the vessel tapering, up to 20% radial reduction was assumed (Itu et al., 2016). An important assumption was that parameter ranges were uniformly distributed corresponding to the worst case scenario as the likelihood of occurence was the same.

The unsteady 3D model was assumed to be the reference model ('golden standard') as it best represents the physiological situation, hence all other models were compared against the reference. The comparison between models was done by investigating the performance for each model and performing uncertainty analysis on geometry parameters. Uncertainty analysis was done in three steps. First, for every combination of CFD models either steady or unsteady, a meta-model was created using the adaptive polynomial chaos expansion (agPCE) method (Quicken et al., 2016) which described the pressure drop for the chosen set of parameters. The main benefit of the agPCE method is the adaptive way meta-models created. Polynomial terms that do increase the meta-model quality significantly are added to the model. On the other hand terms that do not improve meta-model quality are removed. This way only significant terms are kept such that a lower number of CFD model evaluations is needed. Second, these meta-models were evaluated for 10000 samples. Computational costs were substantially lower as new pressure drops within the chosen parameter range could be predicted. Finally, differences in output for the 3D unsteady meta-model and other meta-models were analyzed by comparing the main and total Sobol indices which were computed as described by Quicken et al. (2016). This way, geometrical features causing large pressure drop discrepancies were identified.

2.5. Post-processing

For post-processing, the pressure drop along the centerline was calculated. This was done by generating a plane perpendicular to the centerline for each centerpoint. For each plane along the centerline, the average pressure is computed resulting in a pressure drop along the centerline. The maximum pressure drop was extracted and used to calculate the minimum FFR per geometry. Pressure drops and FFRs obtained from the 2D and 3D models were compared against the reference model. To determine the predictive power of each model, indicators such as the diagnostic accuracy, sensitivity and specificity of each model were investigated.

3. Results

We first compare the results of our models to the findings in literature. Next the models are benchmarked against the unsteady 3D model (reference). Next, the impact of varying seven geometrical characteristics on the predicted FFR and pressure drop for the idealized model are investigated.

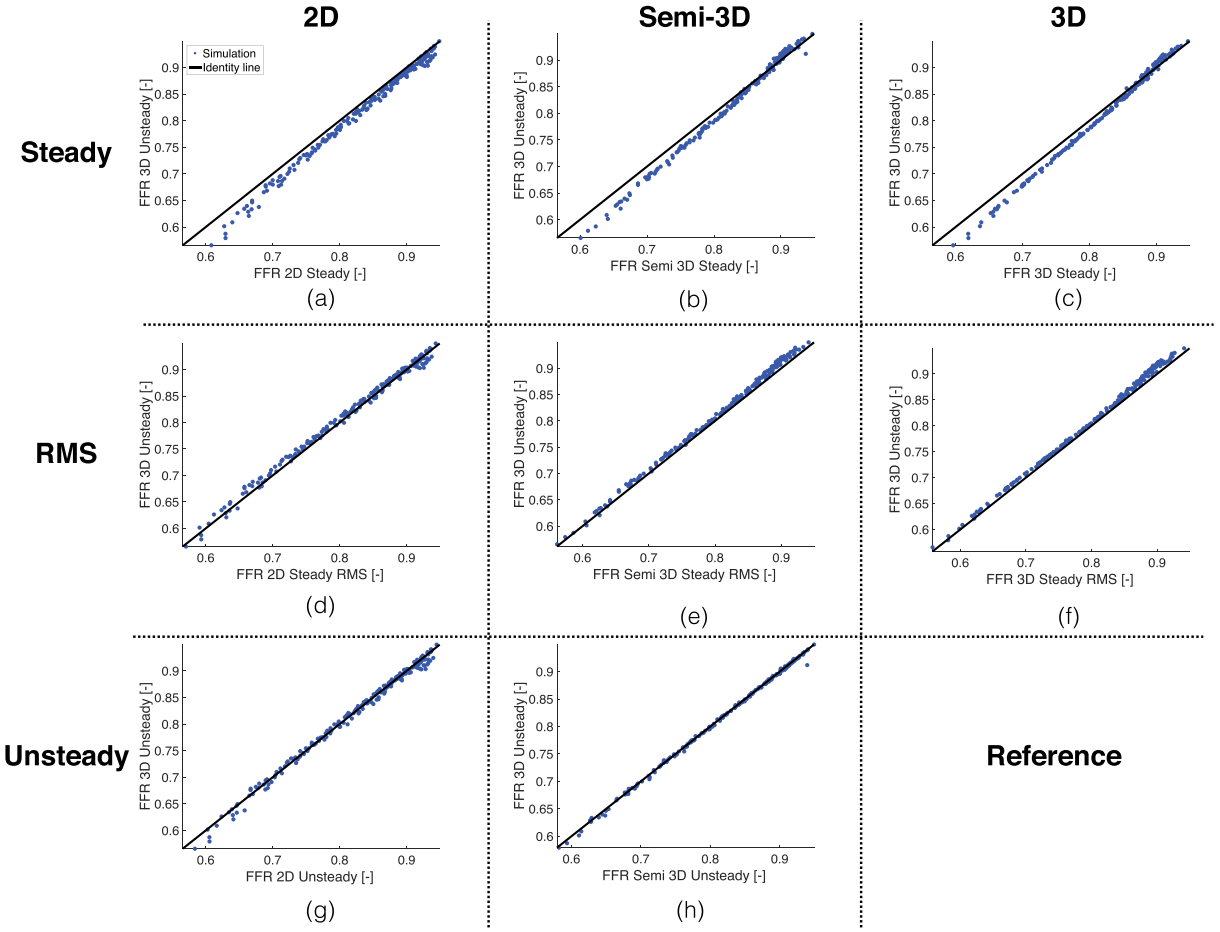

Fig. 5. Computed FFR for all models (2D, Semi-3D and 3D) compared with the results of the 3D unsteady model. On the top row (a, b and c), the predicted FFR of the steady models is shown based on the average flow. On the second row, the results for the steady models with the root mean square of the flow is shown. At the bottom row, the unsteady 2D and Semi-3D model are shown.

3.1. Verification

Simulated hemodynamics were shown to be in good agreement with previous studies (Katritsis et al., 2010; Chang and Tarbell, 1988; Hayashi and Yamaguchi, 2002; Kelidis and Konstantinidis, 2018). For the 2D, Semi-3D and 3D models the recirculation zone was found to increase with increase in stenosis severity (Katritsis et al., 2010; Kelidis and Konstantinidis, 2018). Furthermore, for the Semi-3D and 3D case velocity profiles were found to match the ones found in curved tubes (Chang and Tarbell, 1988; Hayashi and Yamaguchi, 2002; Kelidis and Konstantinidis, 2018).

3.2. Model comparison

Comparison of predicted FFRs for 200 geometries for each model against the 3D unsteady model for both the steady and unsteady case can be seen in Fig. 5. In general, steady models with RMS flow and unsteady models predict the best FFR. Steady mean flow tends to overestimate FFR more with decreasing FFR.

To be able to replace the 3D unsteady model with a computationally less expensive model, the modelling error introduced due to change in model should be lower than the absolute error in FFR measurement reproducibility (Berry et al., 2013 (σ_{FFR}: 0.02); Gaur et al., 2014 (σ_{FFR}: 0.03)). The largest absolute error in predicted FFR is found to be for the steady cases of the Semi-3D and 3D model which is $\sigma = 0.012$ and thus at least 1.6 times smaller than what is found in clinic. The error for the unsteady models (2D, Semi-3D) is shown to be the lowest (Fig. 6). On average, the absolute errors for the 2D and Semi-3D unsteady model are approximately 0.0052 and 0.0018, respectively. As shown before, the error increases for steady mean flow with decreasing FFR. Steady models underestimate the pressure drop by 6%, 6.1% and 7.8% for the 3D, Semi-3D and 2D model, respectively.

The model also should predict the same treatment as the complex 3D unsteady model (FFR cut-off: 0.8). All models are shown to have a sensitivity of at least 0.97 whereas steady models show a sensitivity of 1 when using mean flows (see Table 2). Where steady models with mean flow have the highest sensitivity they also have the lowest specificity (0.93). When using RMS flow, steady models are shown to improve in specificity and PPV whilst maintaining a similar high (> 0.97) sensitivity and NPV (see Table 2). The accuracy of classifying stenoses correctly increases from 95 to 99% when using RMS flow instead of mean flow. For all steady RMS models the accuracy was 0.99 (see Table 2).

The 2D unsteady model has a specificity of 0.98. The diagnostic performance, classifying stenoses correctly, is shown to be at least 0.95. The 2D unsteady model has an accuracy of 0.98 meaning that from the 200 geometries, only 4 geometries were wrongly classified. In general predictions of the steady model with RMS flow are similar to predictions of the 3D unsteady model.

3.3. Uncertainty analysis

Around 170 of the 200 samples were needed to generate accurate meta-models. Furthermore, a maximum polynomial degree of third order (x_i^3) was found in all meta-models whereas interactions

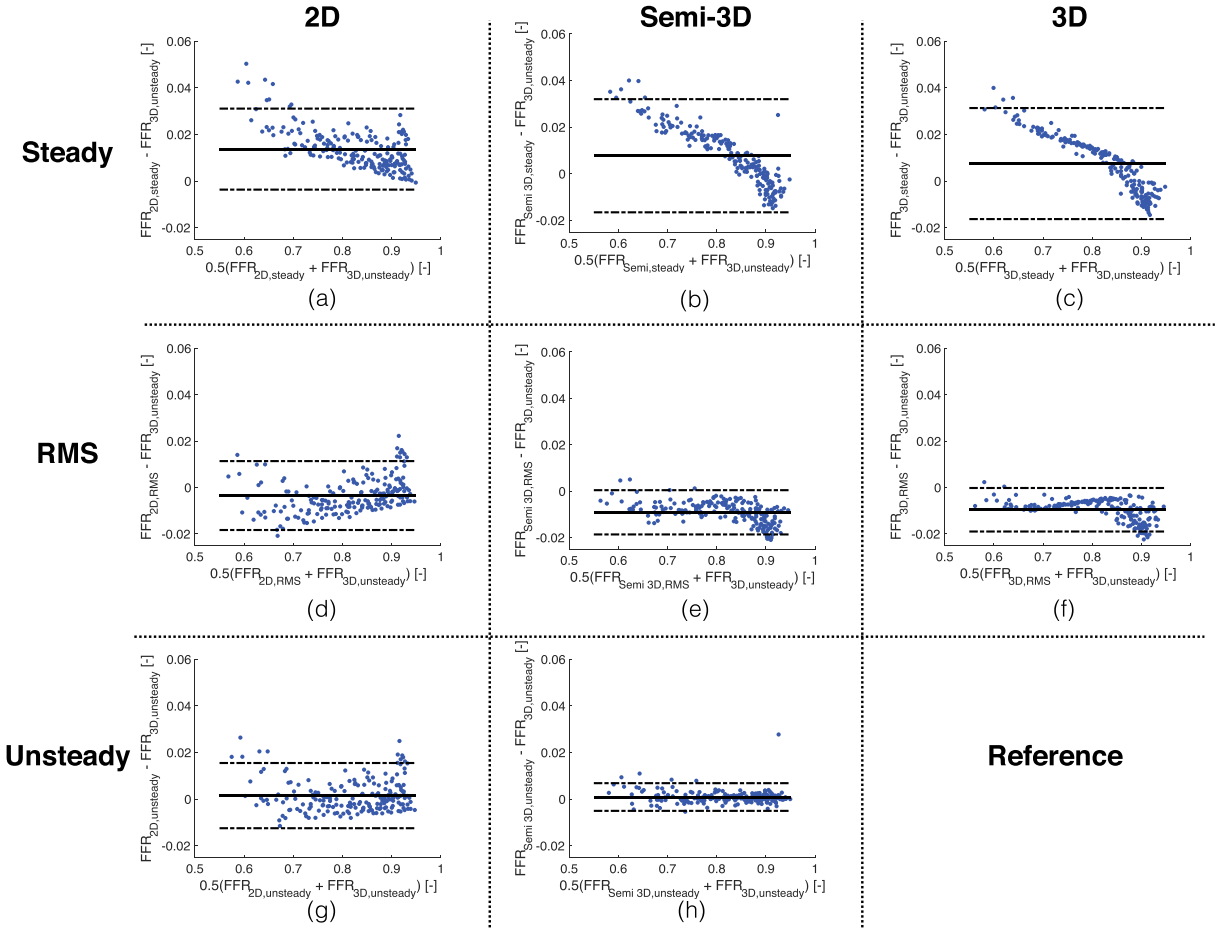

Fig. 6. Differences in computed FFR for all models compared to the reference model shown in Bland–Altman plot. Mean and mean ±1.96 std with the solid and dashed lines, respectively. On the top row, the difference are shown when using a steady model with a mean flow. The second row shows the result for the steady models with root mean square flow. On the bottom row, the differences in computed FFR for the unsteady 2D and Semi-3D models are shown.

Table 2
Performance of the models regarding the sensitivity, specificity, positive predictive value (PPV), negative predictive value (NPV) and accuracy with respect to correct treatment prediction compared to the unsteady 3D model. Furthermore, the average CPU time which is defined as the elapsed real time x the number of cores used is given. Steady 3D and steady semi-3D are solved using the unsteady Navier–Stokes equations, the computational time when solving the steady Navier–Stokes equations is given in brackets which is based on Tu et al. (2014).

Model type	Sensitivity	Specificity	PPV	NPV	Accuracy	CPU time
2D Steady	1.00	0.93	0.88	1.00	0.95	2 s
2D Steady RMS	0.99	0.99	0.99	0.99	0.99	2 s
2D Unsteady	0.99	0.98	0.97	0.99	0.98	28 min
Semi-3D Steady	1.00	0.93	0.88	1.00	0.95	31 h [5 min] (Tu et al., 2014)
Semi-3D Steady RMS	0.97	1.00	1.00	0.98	0.99	33 h [5 min] (Tu et al., 2014)
Semi-3D Unsteady	1.00	0.99	0.99	1.00	0.99	95 h
3D Steady	1.00	0.93	0.88	1.00	0.95	30 h [5 min] (Tu et al., 2014)
3D Steady RMS	0.97	1.00	1.00	0.98	0.99	32 h [5 min] (Tu et al., 2014)
3D Unsteady	–	–	–	–	–	91 h

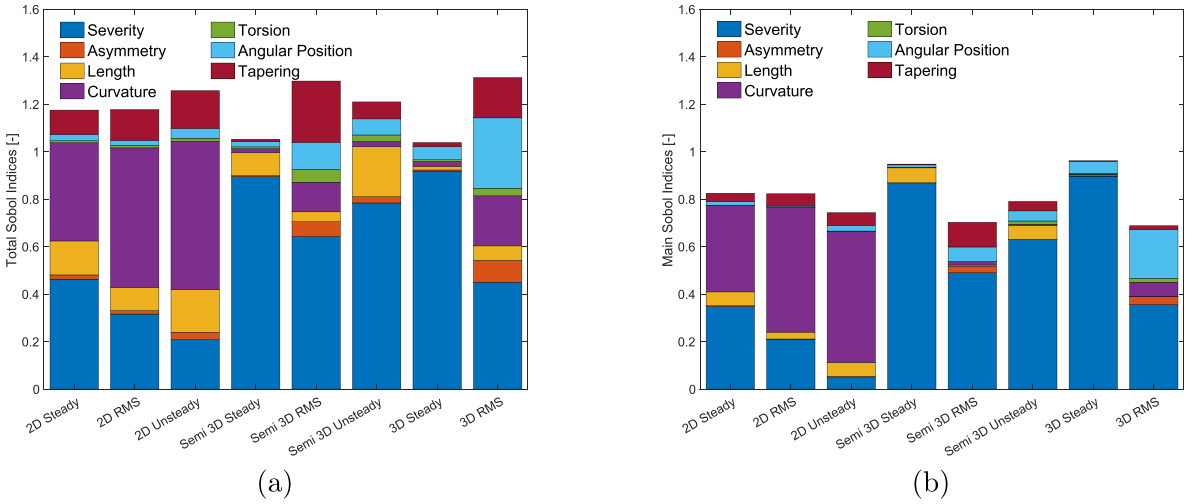

Fig. 7. Main and total Sobol indices for seven parameters for each model benchmarked against the 3D unsteady model.

up to third order ($x_i x_j^2$) were included. For each model different geometrical features are important. In general, differences in output between steady models and the reference model tend to occur mostly due to stenosis severity (Fig. 7). Furthermore, geometry curvature plays a role for 2D models whereas torsion does not play a role at all. Overall, stenosis asymmetry, torsion and angular stenosis position do not influence predictions in FFR. When looking at the total Sobol indices, tapering is shown to be only important when considering 2D models and steady RMS models. Most discrepancies are caused by only four parameters *e.g.* stenosis severity, stenosis length, curvature and vessel tapering. Torsion and angular stenosis position are shown to have an almost negligible effect ($< 5\%$) on FFR differences. Similar is true for the angular position except for the Semi-3D RMS and 3D RMS models.

4. Discussion

The aim of this study was to investigate the effect of replacing the 3D unsteady CFD model with computational less expensive models. Various parametrized geometries were constructed for various 3D geometry characteristics such as stenosis severity, stenosis asymmetry, curvature, etc. Then geometries were simulated with the different models (2D, Semi-3D, 3D). These models were shown to yield results which were in good agreement with previous studies (Katritsis et al., 2010; Kelidis and Konstantinidis, 2018; Chang and Tarbell, 1988; Hayashi and Yamaguchi, 2002; Kelidis and Konstantinidis, 2018). This approach allows ranking characteristics based on their effect on differences in FFR and pressure drops between different CFD models and 3D unsteady model (Reference).

4.1. Model comparison

We showed that when using unsteady models (2D, Semi-3D), predicted pressure drop and FFR match very well with the reference model. However, when using steady models, a corresponding effective flow needs to be chosen. In the current study, we have shown that predicted pressure drop and FFR highly depend on this flow. Steady models overestimate FFR when using mean flow although FFR is defined as a time-averaged quantity (Pijls et al., 1995). This is probably due to the fact that mean flow does not take into account the shape of the flow curve. Contributions of short periods of high flow may be cancelled out when longer periods of low flow or even regurgitant flow occur when only taking the mean of a flow signal. When using the root mean square of the flow curve, the predicted FFR corresponds very well to the 3D unsteady FFR. When using the root mean square, the performance of steady models is shown to get closer to the 3D unsteady model. This can be explained by the fact that the mean flow can be close to zero with sufficient retrograde flow whereas the RMS takes into account the absolute flow curve.

Reducing model complexity yields smaller differences compared to the measured reproducibility in clinic (Berry et al., 2013; Gaur et al., 2014). When using a mean flow for steady models, differences are shown to be slightly above the measured reproducibility for low FFR values. However, for the steady RMS and unsteady models, the differences remain below the reproducibility.

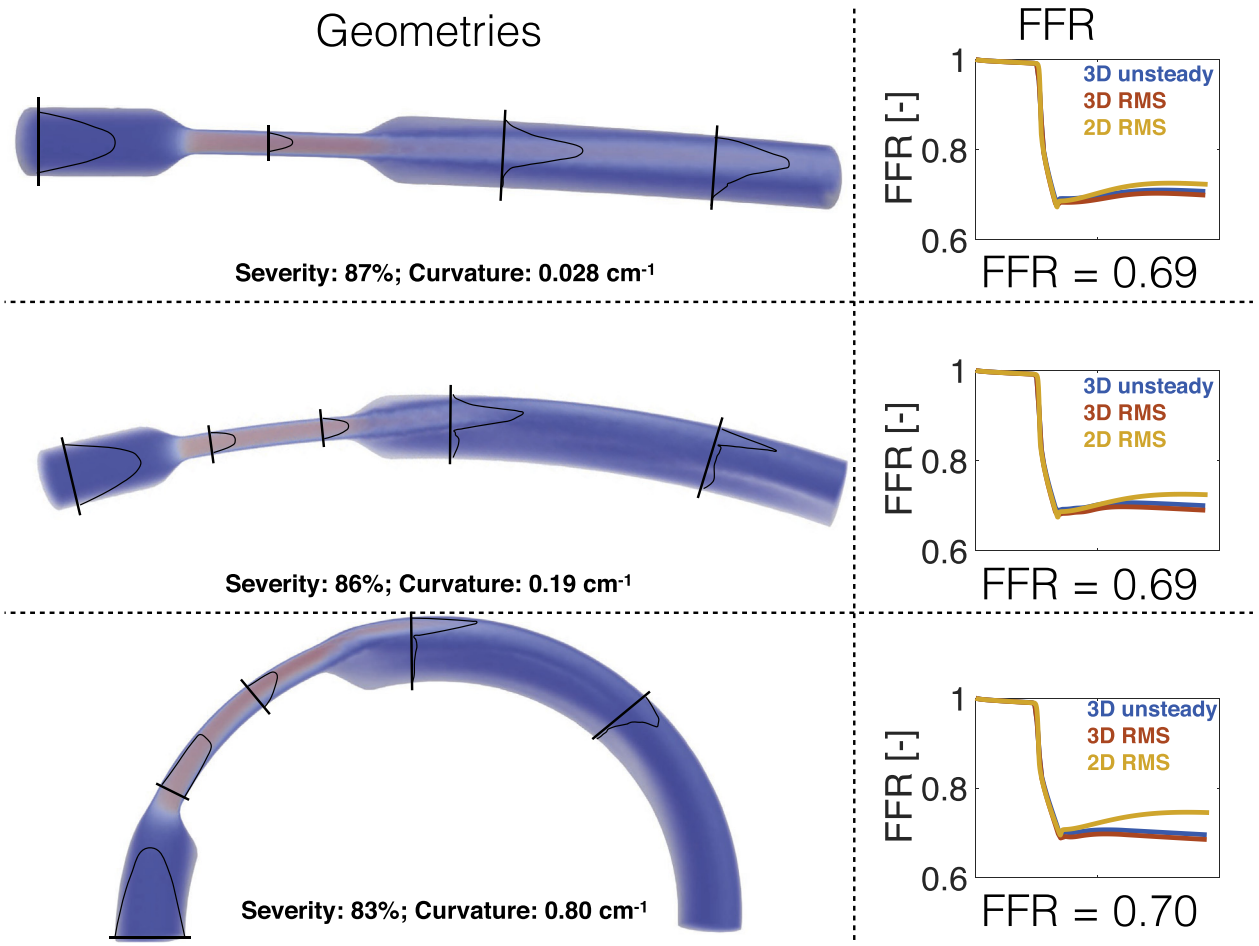

Fig. 8. Schematic overview of three geometries with corresponding velocity profiles and FFRs along the centerline. On the left side geometries with the velocity profile are given with increasing curvature from top to bottom. Furthermore, velocity profiles as a function of the radius are given at multiple locations. Finally at the right side, the FFR as a function of the centerline is depicted for each geometry. This is done for the 3D unsteady (blue), 3D steady RMS (red) and 2D steady RMS (yellow) case.

If we examine the hemodynamics a bit closer, we can see that with increasing curvature the velocity profile changes with high velocity at the outer side of the bend (Chang and Tarbell, 1988; Hayashi and Yamaguchi, 2002; Kelidis and Konstantinidis, 2018) (see Fig. 8). Furthermore, recirculation zones right after the stenosis can be observed which vary in size depending on the stenosis severity similar to what was found in literature (Katritsis et al., 2010; Kelidis and Konstantinidis, 2018).

In this study we have shown three ways of reducing computational time while still maintaining a high diagnostic accuracy. **(1)** Using a full-steady approach where only the steady Navier–Stokes equations are solved for. This effectively reduces the computational effort to the equivalent of solving a couple of time steps which takes around a couple of minutes instead of multiple hours. **(2)** Using a 2D model instead of a Semi-3D or 3D model reduces computational time approximately by a factor 190 while still maintaining a high accuracy. Solving the full-steady 2D model takes on average 2 s to solve for while the 3D unsteady model usually takes around 90 h and thus reduces computational time by a factor 162,000.

4.2. Uncertainty analysis

Uncertainty quantification for the different models shows that the different geometrical features do not influence the models in the same way. When using a 2D model, most of the uncertainty comes from the lack of curvature. This can also be seen in Fig. 8. Although the 2D RMS model is able to capture the same drop in FFR as the 3D unsteady model, it shows a slight post-stenotic overestimation of the FFR. This effect becomes more pronounced when the curvature of the vessel is increased. For the Semi-3D and 3D model, stenosis severity is shown to play an overall dominant role in the uncertainty. On the other hand the role of the stenosis asymmetry, torsion and angular stenosis position is small when reducing the model order. Overall the severity is shown to have a far greater effect than asymmetry and angular stenosis position. This explains why predictions of the 2D and Semi-3D model are so close to the ones of the reference model whilest omitting these geometrical features.

4.3. Limitations

One of the limitations of this study is the fact that parameterized coronary geometries were used. Compared to *in vivo*, current geometries are considered smooth which might influence the predictive power of the models. Nonetheless results of this study are useful for future research using realistic geometries. In this study a proof of concept of the influence of various geometrical features on the predicted FFR is given where specific parts of FFR uncertainty can be attributed to a specific geometrical feature.

Another thing to note is that in this study only one stenosis per vessel is investigated. In future research the currently presented workflow could be extended in a straightforward way for multi stenosed vessels. However, we expect those difference not to change the conclusion regarding the model reduction and parameter importance. The results of this study have shown that given the current input, the 3D unsteady model can be replaced by less computational expensive lower order models.

Conflict of interest statement

None.

Acknowledgment

The authors would like to thank the Dutch institute IMDI-ZonMw for funding [Project number: 104003009].

References

Alnæs, M., Blechta, J., Hake, J., Johansson, A., Kehlet, B., Logg, A., Richardson, C., Ring, J., Rognes, M.E., Wells, G.N., 2015. The fenics project version 1.5. Arch. Numer. Softw. 3, 9–23.

Antiga, L., Piccinelli, M., Botti, L., Ene-Iordache, B., Remuzzi, A., Steinman, D.A., 2008. An image-based modeling framework for patient-specific computational hemodynamics. Med. Biol. Eng. Comput. 46, 1097.

Berry, C., van't Veer, M., Witt, N., Kala, P., Bocek, O., Pyxaras, S.A., McClure, J.D., Fearon, W.F., Barbato, E., Tonino, P.A., et al., 2013. Verify (verification of instantaneous wave-free ratio and fractional flow reserve for the assessment of coronary artery stenosis severity in everyday practice): a multicenter study in consecutive patients. J. Am. Coll. Cardiol. 61, 1421–1427.

Boron, W.F., Boulpaep, E.L., 2012. Medical Physiology, 2e Updated Edition E-Book: with STUDENT CONSULT Online Access. Elsevier Health Sciences.

Chang, L.J., Tarbell, J., 1988. A numerical study of flow in curved tubes simulating coronary arteries. J. Biomech. 21, 927–937.

Chen, S.J., Carroll, J.D., 2000. 3-d reconstruction of coronary arterial tree to optimize angiographic visualization. IEEE Trans. Med. Imaging 19, 318–336.

Çimen, S., Gooya, A., Grass, M., Frangi, A.F., 2016. Reconstruction of coronary arteries from X-ray angiography: a review. Med. Image Anal. 32, 46–68.

De Bruyne, B., Fearon, W.F., Pijls, N.H., Barbato, E., Tonino, P., Piroth, Z., Jagic, N., Mobius-Winckler, S., Rioufol, G., Witt, N., et al., 2014. Fractional flow reserve–guided pci for stable coronary artery disease. N. Engl. J. Med. 371, 1208–1217.

Gaur, S., Bezerra, H.G., Christiansen, E.H., Tanaka, K., Jensen, J.M., Kaltoft, A.K., Botker, H.E., Lassen, J.F., Terkelsen, C.J., Norgaard, B.L., 2014. Reproducibility of invasively measured and non-invasively computed fractional flow reserve. J. Am. Coll. Cardiol. 63, A999.

Gould, K.L., 2009. Does coronary flow trump coronary anatomy? JACC: Cardiovascul. Imaging 2, 1009–1023.

Hall, J.E., 2015. Guyton and Hall Textbook of Medical Physiology e-Book. Elsevier Health Sciences

Hayashi, H., Yamaguchi, T., 2002. A simple computational model of the right coronary artery on the beating heart–effects of the temporal change of curvature and torsion on the blood flow. Biorheology 39, 395–399.

Hulsen, M., 2007. Tfem: A Toolkit for the Finite Element Method.

Itu, L., Rapaka, S., Passerini, T., Georgescu, B., Schwemmer, C., Schoebinger, M., Flohr, T., Sharma, P., Comaniciu, D., 2016. A machine-learning approach for computation of fractional flow reserve from coronary computed tomography. J. Appl. Physiol. 121, 42–52.

Johnson, N.P., Kirkeeide, R.L., Gould, K.L., 2013. Coronary anatomy to predict physiology: fundamental limits. Circulat.: Cardiovascul. Imaging 6, 817–832.

Katritsis, D., Theodorakakos, A., Pantos, I., Andriotis, A., Efstathopoulos, E., Siontis, G., Karcanias, N., Redwood, S., Gavaises, M., 2010. Vortex formation and recirculation zones in left anterior descending artery stenoses: computational fluid dynamics analysis. Phys. Med. Biol. 55, 1395.

Kelidis, P., Konstantinidis, E., 2018. Pulsatile flow through a constricted tube: effect of stenosis morphology on hemodynamic parameters. Comput. Methods Biomech. Biomed. Eng. 21, 479–487.

Kim, K.H., Doh, J.H., Koo, B.K., Min, J.K., Erglis, A., Yang, H.M., Park, K.W., Lee, H.Y., Kang, H.J., Kim, Y.J., et al., 2014. A novel noninvasive technology for treatment planning using virtual coronary stenting and computed tomography-derived computed fractional flow reserve. JACC: Cardiovascul. Intervent. 7, 72–78.

Koo, B.K., Erglis, A., Doh, J.H., Daniels, D.V., Jegere, S., Kim, H.S., Dunning, A., DeFrance, T., Lansky, A., Leipsic, J., et al., 2011. Diagnosis of ischemia-causing coronary stenoses by noninvasive fractional flow reserve computed from coronary computed tomographic angiograms: results from the prospective multicenter discover-flow (diagnosis of ischemia-causing stenoses obtained via noninvasive fractional flow reserve) study. J. Am. Coll. Cardiol. 58, 1989–1997.

Miller, D.D., Donohue, T.J., Younis, L.T., Bach, R.G., Aguirre, F.V., Wittry, M.D., Goodgold, H.M., Chaitman, B.R., Kern, M.J., 1994. Correlation of pharmacological 99mtc-sestamibi myocardial perfusion imaging with poststenotic coronary flow reserve in patients with angiographically intermediate coronary artery stenoses. Circulation 89, 2150–2160.

Min, J.K., Leipsic, J., Pencina, M.J., Berman, D.S., Koo, B.K., van Mieghem, C., Erglis, A., Lin, F.Y., Dunning, A.M., Apruzzese, P., et al., 2012. Diagnostic accuracy of fractional flow reserve from anatomic ct angiography. Jama 308, 1237–1245.

Min, J.K., Taylor, C.A., Achenbach, S., Koo, B.K., Leipsic, J., Nørgaard, B.L., Pijls, N.J., De Bruyne, B., 2015. Noninvasive fractional flow reserve derived from coronary ct angiography: clinical data and scientific principles. JACC: Cardiovascul. Imaging 8, 1209–1222.

Morris, P.D., Ryan, D., Morton, A.C., Lycett, R., Lawford, P.V., Hose, D.R., Gunn, J.P., 2013. Virtual fractional flow reserve from coronary angiography: modeling the significance of coronary lesions: results from the virtu-1 (virtual fractional flow reserve from coronary angiography) study. JACC: Cardiovascul. Intervent. 6, 149–157.

Morris, P.D., van de Vosse, F.N., Lawford, P.V., Hose, D.R., Gunn, J.P., 2015. Virtual (computed) fractional flow reserve: current challenges and limitations. JACC: Cardiovascul. Intervent. 8, 1009–1017.

Morris, P.D., Narracott, A., von Tengg-Kobligk, H., Soto, D.A.S., Hsiao, S., Lungu, A., Evans, P., Bressloff, N.W., Lawford, P.V., Hose, D.R., et al., 2016. Computational fluid dynamics modelling in cardiovascular medicine. Heart 102, 18–28.

Morris, P.D., Soto, D.A.S., Feher, J.F., Rafiroiu, D., Lungu, A., Varma, S., Lawford, P.V., Hose, D.R., Gunn, J.P., 2017. Fast virtual fractional flow reserve based upon steady-state computational fluid dynamics analysis: results from the virtu-fast study. JACC: Basic Transl. Sci. 2, 434–446.

Mortensen, M., Valen-Sendstad, K., 2015. Oasis: a high-level/high-performance open source Navier–Stokes solver. Comput. Phys. Commun. 188, 177–188.

Nakazato, R., Park, H.B., Berman, D.S., Gransar, H., Koo, B.K., Erglis, A., Lin, F.Y., Dunning, A.M., Budoff, M.J., Malpeso, J., et al., 2013. Noninvasive fractional flow reserve derived from computed tomography angiography for coronary lesions of intermediate stenosis severity: results from the defacto study. Circulat.: Cardiovascul. Imaging 6, 881–889.

Nørgaard, B.L., Leipsic, J., Gaur, S., Seneviratne, S., Ko, B.S., Ito, H., Jensen, J.M., Mauri, L., De Bruyne, B., Bezerra, H., et al., 2014. Diagnostic performance of noninvasive fractional flow reserve derived from coronary computed tomography angiography in suspected coronary artery disease: the nxt trial (analysis of coronary blood flow using ct angiography: next steps). J. Am. Coll. Cardiol. 63, 1145–1155.

Pijls, N.H., Van Gelder, B., Van der Voort, P., Peels, K., Bracke, F.A., Bonnier, H.J., El Gamal, M.I., 1995. Fractional flow reserve. Circulation 92, 3183–3193.

Pijls, N.H., van Schaardenburgh, P., Manoharan, G., Boersma, E., Bech, J.W., vantVeer, M., Bär, F., Hoorntje, J., Koolen, J., Wijns, W., et al., 2007. Percutaneous coronary intervention of functionally nonsignificant stenosis: 5-year follow-up of the defer study. J. Am. Coll. Cardiol. 49, 2105–2111.

Quicken, S., Donders, W.P., van Disseldorp, E.M., Gashi, K., Mees, B.M., van de Vosse, F.N., Lopata, R.G., Delhaas, T., Huberts, W., 2016. Application of an adaptive polynomial chaos expansion on computationally expensive three-dimensional cardiovascular models for uncertainty quantification and sensitivity analysis. J. Biomech. Eng. 138, 121010.

Sankaran, S., Grady, L., Taylor, C.A., 2015. Fast computation of hemodynamic sensitivity to lumen segmentation uncertainty. IEEE Trans. Med. Imaging 34, 2562–2571.

Sankaran, S., Kim, H.J., Choi, G., Taylor, C.A., 2016. Uncertainty quantification in coronary blood flow simulations: impact of geometry, boundary conditions and blood viscosity. J. Biomech. 49, 2540–2547.

Segal, G., 1989. The sepran finite element package. Ingenieursburo Sepra, Leidschendam, The Netherlands.

Stary, H.C., Chandler, A.B., Dinsmore, R.E., Fuster, V., Glagov, S., Insull, W., Rosenfeld, M.E., Schwartz, C.J., Wagner, W.D., Wissler, R.W., 1995. A definition of advanced types of atherosclerotic lesions and a histological classification of atherosclerosis. Circulation 92, 1355–1374.

Tang, D., Yang, C., Kobayashi, S., Zheng, J., Woodard, P.K., Teng, Z., Billiar, K., Bach, R., Ku, D.N., 2009. 3d mri-based anisotropic fsi models with cyclic bending for human coronary atherosclerotic plaque mechanical analysis. J. Biomech. Eng. 131, 061010.

Taylor, C.A., Fonte, T.A., Min, J.K., 2013. Computational fluid dynamics applied to cardiac computed tomography for noninvasive quantification of fractional flow reserve. J. Am. Coll. Cardiol. 61, 2233–2241.

Tonino, P.A., De Bruyne, B., Pijls, N.H., Siebert, U., Ikeno, F., vant Veer, M., Klauss, V., Manoharan, G., Engstrøm, T., Oldroyd, K.G., et al., 2009. Fractional flow reserve versus angiography for guiding percutaneous coronary intervention. N. Engl. J. Med. 360, 213–224.

Tonino, P.A., Fearon, W.F., De Bruyne, B., Oldroyd, K.G., Leesar, M.A., Ver Lee, P.N., MacCarthy, P.A., Van't Veer, M., Pijls, N.H., 2010. Angiographic versus functional severity of coronary artery stenoses in the fame study: fractional flow reserve versus angiography in multivessel evaluation. J. Am. Coll. Cardiol. 55, 2816–2821.

Tu, S., Barbato, E., Köszegi, Z., Yang, J., Sun, Z., Holm, N.R., Tar, B., Li, Y., Rusinaru, D., Wijns, W., et al., 2014. Fractional flow reserve calculation from 3-dimensional quantitative coronary angiography and timi frame count. JACC: Cardiovascul. Intervent. 7, 768–777.

Waksman, R., Prati, F., Bruining, N., Haude, M., Böse, D., Kitabata, H., Erne, P., Verheye, S., Degen, H., Vermeersch, P., et al., 2013. Serial observation of drug-eluting absorbable metal scaffold: multi-imaging modality assessment. Circulat.: Cardiovascul. Intervent. 6, 644–653.

Wei, K., Ragosta, M., Thorpe, J., Coggins, M., Moos, S., Kaul, S., 2001. Noninvasive quantification of coronary blood flow reserve in humans using myocardial contrast echocardiography. Circulation 103, 2560–2565.

Wilson, R.F., Johnson, M.R., Marcus, M.L., Aylward, P., Skorton, D.J., Collins, S., White, C.W., 1988. The effect of coronary angioplasty on coronary flow reserve. Circulation 77, 873–885.